

Article

Investigation on Stranski–Krastanow (SK) Growth Mode of Ag Coating in Cu/Ag Core-Shell Composites

Xingyuan Wan , Yiyong Wang *, Jinlin Lu, Zhe Ning and Jidong Li

School of Materials & Metallurgy, University of Science and Technology Liaoning, Anshan 114051, China; wanxingyuan2017@163.com (X.W.); jinlinlu@hotmail.com (J.L.); classcl@126.com (Z.N.); lijidong1014@163.com (J.L.)

* Correspondence: wangyiyongfly@163.com; Tel.: +86-412-5929559

Received: 20 February 2020; Accepted: 18 March 2020; Published: 23 March 2020



Abstract: Cu/Ag core-shell composite was synthesized by the replacement-reduction method and was applied to the catalytic field. The specimens were analyzed by X-ray diffraction (XRD), scanning electron microscopy (SEM), and transmission electron microscope (TEM). The growth mechanism was investigated by the first-principles calculation, including the density of states, Mulliken population, and electronic structures. By comparing the calculation and characterization, it is concluded that the difference in interfacial properties leads to the growth of silver on the copper surface in the Stranski–Krastanow (SK) mode.

Keywords: density functional theory; composites; catalyst; growth mode

1. Introduction

Precious metals such as gold, platinum, and palladium are widely used in organic synthesis and the fuel cell [1–4]. The synthesis and surface modification of nano precious metal particles has become one of the hot topics in the catalytic field. However, precious metal materials are expensive to manufacture, especially nanoscale particles [5,6]. Furthermore, it is found that copper nanoparticles are used for catalytic synthesis. The copper nanoparticles are considered to be an ideal replacement for precious metal catalysts [7]. However, copper has obvious defects, that is, it is easily oxidized, resulting in a deactivation and seriously affecting catalytic efficiency. The price of silver is that of far from most precious metals and its properties are similar to precious metals. Therefore, the Ag coating on the surface of copper particles not only prevents the oxidation of copper but also preserves the catalytic efficiency [8].

It is well known that silver can be deposited by electroplating, but the electroplating on the surface of particles is difficult due to the low efficiency. Therefore, the displacement reaction was used to synthesize the core-shell composites owing to the different reduction potential between Cu and Ag. (The standard potential in aqueous solution at 25 °C versus normal hydrogen electrode is 0.779 V for Ag and 0.340 V for Cu). The reaction between Cu and Ag⁺ is the key step in the synthesis. Therefore, complexing agents, such as ethylenediaminetetraacetic acid (EDTA), ammonium hydroxide (NH₃·H₂O), sodium thiosulfate (Na₂S₂O₃), are used to inhibit the rate [9]. However, Cu²⁺ produced by the reaction easily reacts with the complexing agent, and copper has a strong adsorption effect on the complex ions, preventing further copper replacement. Another method is to use a reducing agent to reduce Ag⁺ from the plating solution and use copper atom nucleation centers to gradually grow silver particles on the surface of the copper powder to obtain a continuous coating. However, the stability of the plating solution is poor. Especially when a strong reducing agent is present, the plating solution is easily decomposed. In addition, the electroless plating reaction rate is fast, it is not easy to control, and related research work is lacking [10].

The morphology of particles is related to the catalytic properties, so the growth mode of the coating has attracted great attention. Heteroepitaxial growth has been demonstrated in film materials, which is dependent on the lattice mismatch between the coating and the substrate [11,12]. In core-shell composites, the HRTEM images of the interface were used to investigate the deposition of the coating. It is reported that the growth of Ag coating on Cu nanowires confirms to heteroepitaxial growth, and the Ag shell retains the same crystallographic orientation and twin structure as Cu nanowires [13]. However, for spherical particles, the growth mode of shell and the relationship between the substrate and the coating are not clear. First-principles calculations can simulate the growth of coatings, but there is no quasi-deterministic method for the calculation of core-shell models. Non-periodic or low-periodic core-shell models are used to explore the growth mechanism of the shell, but this is obviously different from reality, and the calculation results are not suitable for large-scale material systems [14].

In this study, we reported a new method for preparing Cu/Ag core-shell particles and investigated the growth mechanism of Ag coatings by first-principles. By establishing a periodic model in the x , y , z directions, the properties of the Cu/Ag interface were analyzed, and the results were compared with the characterization results to verify the accuracy of the calculation. The Cu/Ag core-shell synthesized by this method has potential for application in many fields, and provides a theoretical reference for the synthesis and design of core-shell composites.

2. Materials and Methods

2.1. Synthesis of Copper Particles

All chemicals in the experiments were of analytical grade and were used without further purification. In the synthesis of copper particles, 500 mL aqueous solution was stirred at 120 °C for 6 h in an autoclave (Anhui Kemi Machinery Technology Co., Ltd., Anhui, China) with a total volume of 1 L. The concentrations of cupric oxide (CuO), sodium hydroxide (NaOH), and glucose (C₆H₁₂O₆) in the solution were 72, 72, and 189 g/L, respectively. After the autoclave was cooled to room temperature, the copper particles were collected by centrifugation at 5000 r/min, washed 3 times with distilled water, and 5 times with ethanol, and were then vacuum dried at 70 °C for 10 h.

2.2. Synthesis of Cu/Ag Core-Shell Composites

Copper powder is easily oxidized during drying and storage, so pickling must be performed before the composites are synthesized. In total, 100 mL of 10% dilute sulfuric acid, 100 mL of absolute ethanol, and 4 g of copper particles were stirred in a water bath at 60 °C for 30 min. After pickling, copper particles were collected by centrifugation at 5000 r/min and washed 3 times with distilled water. Then, the wet copper particles were added to 200 mL of 5% dilute aqueous ammonia at 60 °C, and 2.5 g of glucose powder was further added to the mixed solution. Finally, a freshly prepared silver ammonia solution (Ag(NH₃)₂OH) was slowly dropped into the mixed solution using a peristaltic pump. In a typical silver ammonia solution synthesis, one would add 3 drops of 10% sodium hydroxide solution (NaOH) to 100 mL of 4% silver nitrate solution (AgNO₃), and add 25% concentrated ammonia water (NH₃·H₂O) until precipitation. Mechanical agitation and ultrasonic oscillation were maintained during the synthesis in order to eliminate the agglomeration of ultrafine particles.

2.3. Characterization of Specimen

The X-ray diffraction technique (X'Pert Powder, PANalytical, Almelo, The Netherlands) was used to analyze the phase composition (Cu K α filtered radiation, step = 0.02°, scanning speed = 10°/min, 2 theta ranged from 10° to 100°). The morphological features were complemented by scanning electron microscopy (SEM) (1 KV~15 KV, Zeiss-SIGMA HD, Carl Zeiss, Oberkochen, Germany) and transmission electron microscopy (TEM) (200 KV, JEM-2100F, JEOL, Tokyo, Japan).

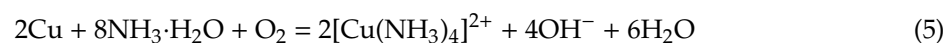
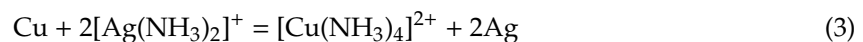
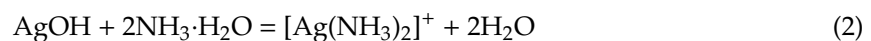
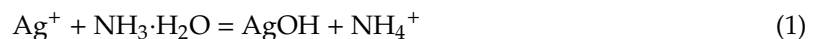
2.4. Method of Calculation

All calculations were performed by a first-principles method on density functional theory (DFT), as implemented in the Cambridge series total energy package (CASTEP) code. The generalized gradient approximations (GGA) of the Perdew–Burke–Ernzerhof (PBE) approach were implemented to describe the exchange–correlation functional. The cut-off energy of the plane-waves basis set used to represent the balance electron was 351.00 eV. The k-point sampling grids obtained by using the Monkhorst–Pack method were set to $8 \times 8 \times 8$ and $8 \times 8 \times 1$ for the bulk and all slabs. All atoms were relaxed to their equilibrium position, where the optimization period always changed to a final convergence of less than 5.0×10^{-6} eV/atom. The forces on all atoms were minimized to less than 0.01 eV/Å, stress was clobbered to 0.01 GPa on each atom, and the displacement was converted to 5×10^{-4} Å [15]. Using the Broyden–Fletcher–Goldfarb–Shannon (BFGS) algorithm to automatically relax the internal coordinates of the atom means that the system can always be minimized. The super-soft pseudo-potentials were utilized to describe the interaction between the ion nucleus and valence electrons. For the Cu and Ag, the valence electrons considered in their pseudopotential were Cu $3d^{10}4s^1$ and Ag $4d^{10}5s^1$. The surfaces and interfaces were modeled by the supercell method with periodic boundary conditions, and the thickness of the vacuum layer was 15.0 Å.

3. Results

3.1. Characterization of Specimens

Ag has a higher reduction potential than Cu, and Ag^+ ions are reduced into Ag atoms by transforming Cu atoms into Cu^{2+} . However, Ag^+ ions are present in a glucose-rich alkaline solution. There is a direct reduction reaction of Ag^+ ions, which is called a “replacement-reduction” method. The chemical equations for silver ammonia solution and silver deposition are as follows [16,17]:



Cu and Ag are almost immiscible at room temperature, but Cu is the faster diffusion species in the Cu/Ag diffusion couple. Cu atoms at the Cu/Ag interface diffuse to the Ag surface and exchange with Ag^+ ions by leaving vacancies at the interface as a result of the Kirkendall effect. In this paper, the key to inhibit the Kirkendall effect is to add 5% dilute ammonia to inhibit the displacement reaction. Since the $[\text{Cu}(\text{NH}_3)_4]^{2+}$ ion is generated, the Equation (3) is inhibited during the coating process.

The Cu/Ag core-shell composite replicate the spherical structure of the Cu particles (Figure 1a,b), while the particle size distribution of specimens show that the two materials have similar average particle sizes (227.17 nm for Cu, 234.96 nm for Cu/Ag core-shell composite), but the size of Cu/Ag core-shell composite is slightly larger than the Cu particles (Figure 1i). Considering the agglomeration properties of the nanoparticles, for each sample, a large number of SEM images were measured, then 2000 particles were randomly selected for measurement and statistics, and the particle size distribution map was finally drafted. This phenomenon proves once again that Equation (3) is effectively inhibited, and the reduction reaction of Ag^+ ions mainly occurs in the solution. X-ray diffraction (XRD) measurements were made on the specimens to assess the structure and phase purity. The diffraction peaks can be indexed to a Copper, syn structure of Cu, Copper, syn, and Silver-3C, syn structure of Cu/Ag core-shell composite, as shown in Figure 1c. No diffraction peaks from impurities were found in the specimens. These results provide parameters for the simulations below. However,

the peaks of the Cu/Ag core-shell composite are significantly broadened, demonstrating that the crystallinity of the material deteriorated. To ascertain the core-shell structure, the TEM and SEM-EDS cross-sectional images are presented in Figure 1g. In Figure 1e,f, the TEM image of the specimen confirms that it is indeed a core-shell structure, and the average thickness of the shell layer is about 40 nm. The SAED and EDS patterns further confirm the core-shell structure and the components. In Figure 1g, there is a strong intensity of copper on the core and a weak intensity of silver on the shell, and the composites contain 21.86 wt.% of Ag, 78.14 wt.% of Cu. (The background value of the epoxy resin has been removed). The above characterization results are similar to those in the literature, proving that the material synthesis is successful [13].

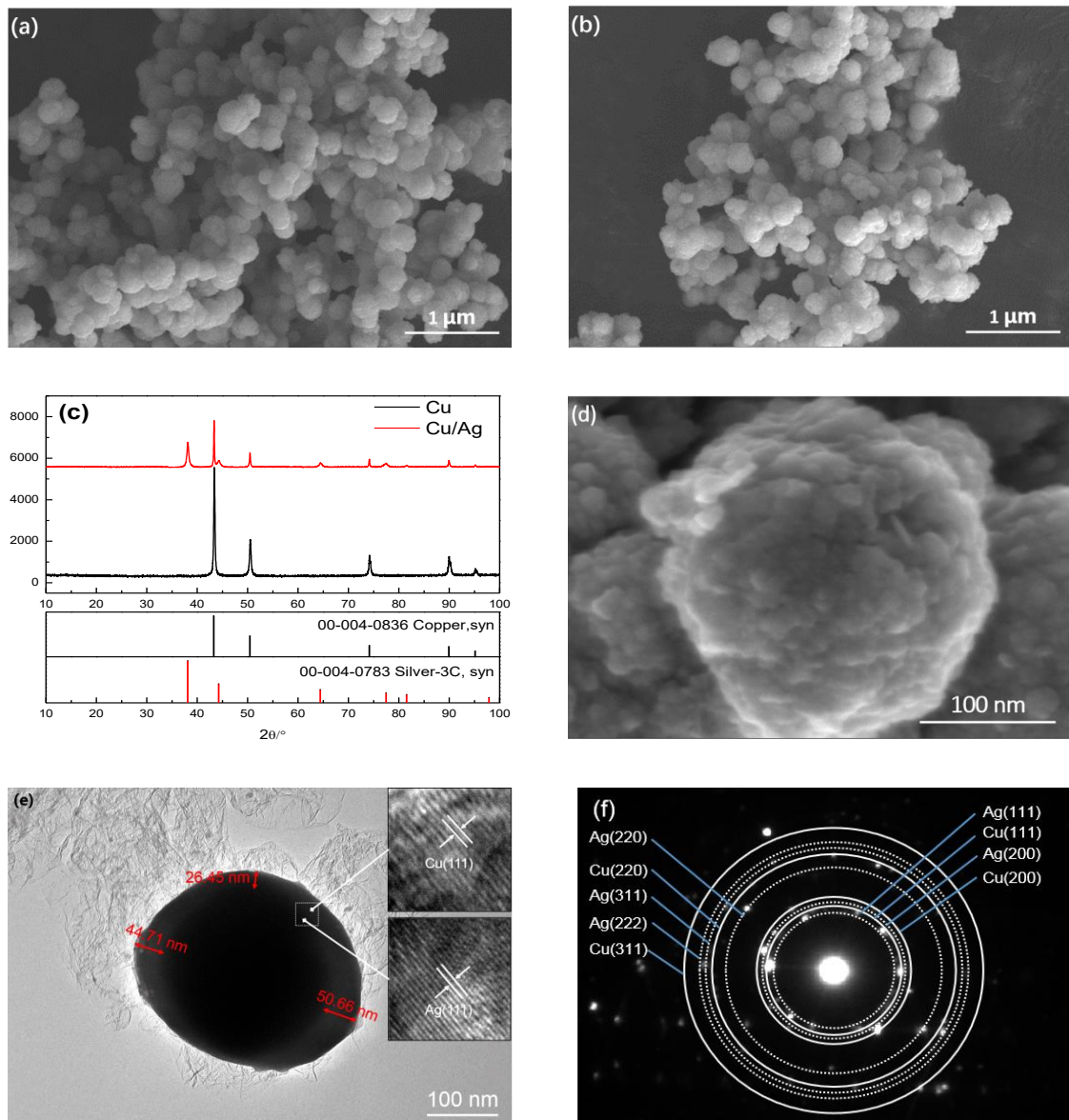


Figure 1. Cont.

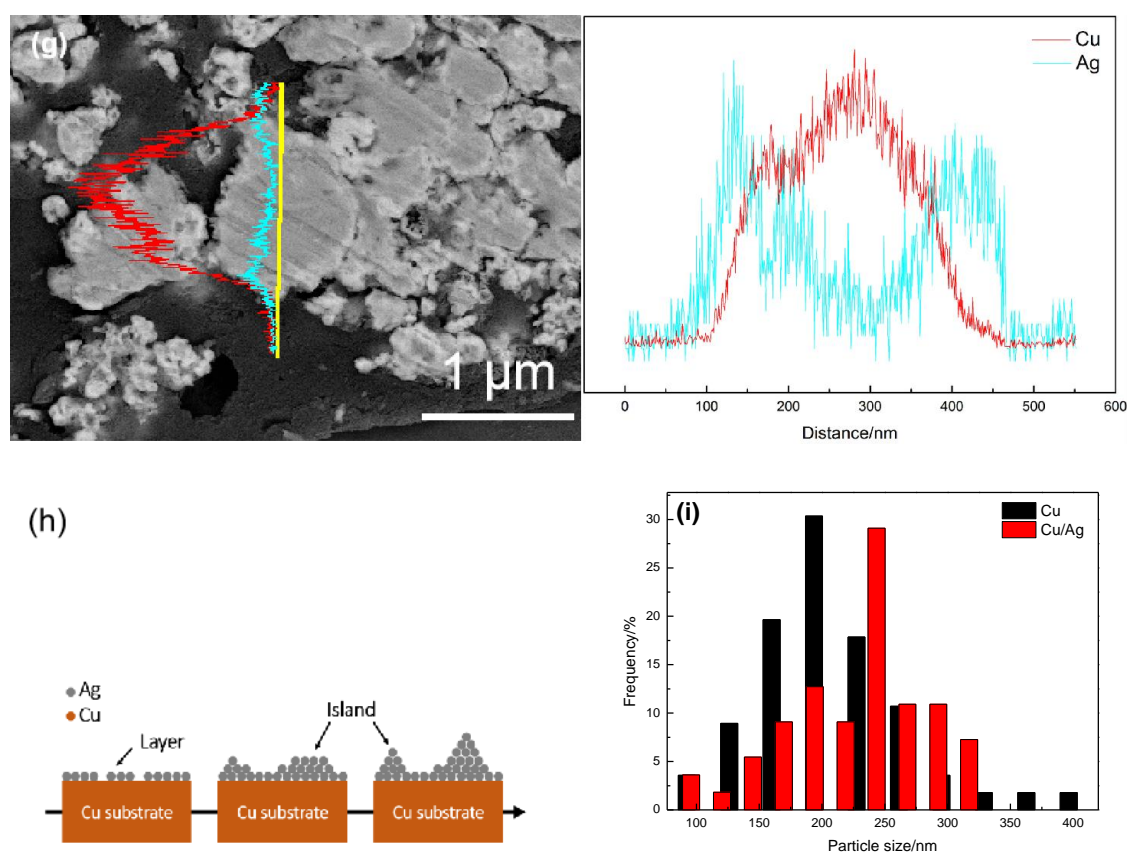


Figure 1. (a) Scanning electron microscope (SEM) image of Cu particles; (b) an SEM image of Cu/Ag core-shell composite; (c) X-ray diffraction (XRD) patterns of Cu particles and Cu/Ag core-shell composite; (d) a high magnification SEM image of Cu/Ag core-shell composite; (e) a transmission electron microscope (TEM) image of Cu/Ag core-shell composite; (f) SAED patterns of Cu/Ag core-shell composite; (g) an SEM cross-section image of Cu/Ag core-shell composite; (h) a schematic diagram of the growth mode of the silver coating; (i) the particle size distribution of Cu and Cu/Ag core-shell composite.

For low-dimensional Cu/Ag core-shell structures, there are three heteroepitaxial growth modes of Ag coating, namely the Frank–Van der Merwe (FM) mode, the Volmer–Weber (VW) mode, and Stranski–Krastanow (SK) mode. In this work, Ag grows in a three-dimensional space, so whether the growth of Ag proceeds in the SK mode remains to be verified. The schematic diagram of SK growth mode is shown in Figure 1h. The growth mode of the epitaxial layer depends on the free energy of the system, and also reflects the competitive balance between strain energy and surface energy and interface energy. Therefore, the experimental conclusion can be verified by calculating the energy relationship of the interface system by the first principles [18].

3.2. Geometric Optimization

Based on the speculation obtained above, a Cu/Ag interface model was established to calculate interface properties and verify the growth mode. As the modeling method of the Cu/Ag core-shell system is seldom reported in the literature, in order to ensure that the simulation calculation is closer to the actual situation and the calculation result can be applied to a larger scale, a vacuum slab model is used. This does not change the periodicity of Cu and Ag, and does not limit the physical size of the material, making the calculation more convincing and universal.

For the choice of atomic layers, it is necessary to satisfy that the atoms in the depth of the surface have bulk atomic characteristics. On the other hand, with the increase in atomic layers, the computational time will increase. Therefore, the number of atomic layers in each surface model

is taken as 5 layers. Since the spherical particles grow in all directions of space, one-dimensional, two-dimensional, and three-dimensional directions are selected separately when the model is built. Establishing representative (111), (110), and (100) surface models in the [111], [110], and [100] directions can be closer to the actual situation. The surface energy is calculated after geometric optimization, which is shown in Table 1. In density functional theory, surface energy can be calculated from the following expression [19]:

$$E_{sur} = \frac{E_{slab} - nE_{bulk}}{2A} \quad (6)$$

where E_{slab} is the total energy of surface slab obtained using density functional theory. n is the number of atoms in the surface slab. E_{bulk} is the bulk energy per atom. A is the surface area. For a slab, we have two surfaces and they are of the same type, which is reflected by the number 2 in the denominator.

Table 1. Surface energy after geometric optimization.

Species	Surface	E_{slab} (eV)	E_{bulk} (eV)	n	A (\AA^2)	E_{sur} (eV)	E_{sur} (J/m ²)
Cu	(111)	-7381.8278	-1472.4135	5	5.6585	-1.7461	-27.9370
	(110)	-14,763.6947	-1472.4135	10	9.2406	-2.1405	-34.2485
	(100)	-14,764.3335	-1472.4135	10	6.5341	-3.0761	-49.2168
Ag	(111)	-5136.5884	-1024.6651	5	7.2298	-0.9172	-14.6758
	(110)	-10,273.4678	-1024.6651	10	11.8066	-1.1357	-18.1707
	(100)	-10,273.9832	-1024.6651	10	8.3485	-1.6370	-26.1912

Figure 2 displays the interface models and evaluating the relatively stable interface model by calculating the interface binding energy, the density of states and population. For each set of images, the model below is the geometric optimization result of the above. For Cu(111), Cu(110), and Cu(100), their surface energy varies considerably, which proves that the active sites on the surface of Cu particles are unevenly distributed. This difference in activity influences the rate of reaction, resulting in vacancies on the surface.

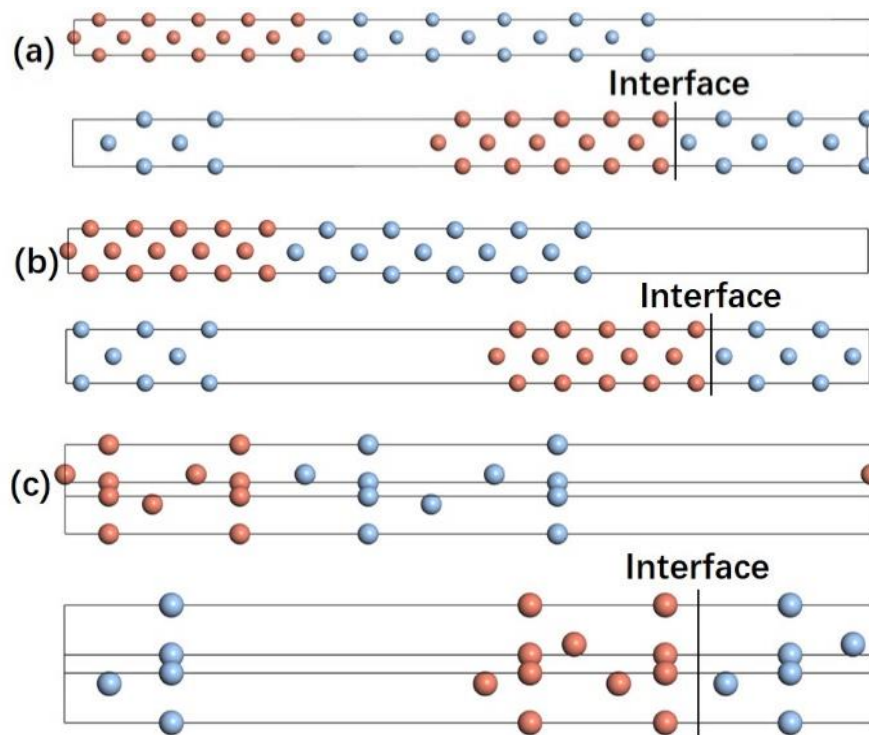


Figure 2. The structures of the Cu/Ag interface. (a) Ag(100)/Cu(100); (b) Ag(110)/Cu(110); (c) Ag(111)/Cu(111).

The stability and combination of the interface are usually expressed by the interface energy, as given in Equation (7) [20].

$$\gamma_{int} = \frac{(E_{Ag} + E_{Cu} - E_{Cu/Ag})}{A} \quad (7)$$

where E_{Ag} and E_{Cu} denote the total energies of the Ag(hkl) slab and the Cu(hkl) slab with five atomic layers, respectively, $E_{Cu/Ag}$ is the total energies of Cu/Ag slab, and A is the interface area.

The interface energy is shown in Table 2. In the absence of special instructions, the comparison between energy does not take into account the sign. The order of the absolute values of interface energy indicates that the Ag(100)/Cu(100) interface is the most stable structure.

Table 2. The work of adhesion and interface energy at the Ag/Cu interface.

Interface	$\gamma_{int}/\text{eV}\cdot\text{\AA}^2$	$A/\text{\AA}^2$	Bond Length/ \AA
Ag(111)/Cu(111)	0.2452	6.9218	2.9372
Ag(110)/Cu(110)	0.4996	9.1618	2.6709
Ag(100)/Cu(100)	0.5425	8.1644	2.6459

The total free energy of the model determines the growth pattern of the Ag coating, usually represented by Equation (8) [21]. However, the correspondence between the growth mode and the free energy of the model is not clear, and the calculation of strain energy is difficult. Therefore, the growth mode of the coating is determined by calculating the energy relationship between the substrate, the coating, and the interface.

$$F = E_{strain} + \sigma + \gamma_{int} \quad (8)$$

where F denotes the total free energy of the model, E_{strain} is the strain energy of the model, σ is the surface energy of the model, and γ_{int} is the interface energy of the model.

According to the data in Table 2, the energy relationship between the substrate, the coating, and the interface can be obtained, which is presented in Table 3. The surface energy of the substrate (σ_{Cu}) is greater than the sum of the surface energy of the coating (σ_{Ag}) and the interface energy (γ_{int}). It is found that the interface energy is small, and the epitaxial material atoms are distributed on the substrate, and a thin strain layer is formed on the surface in the pre-stage. As the epitaxial growth progresses, the elastic strain in the epitaxial layer increases as the layer thickness increases. When the thickness of the epitaxial layer is raised to a certain value, the strain energy accumulated in the strained layer is released by redistributing the atoms reaching the surface to form a three-dimensional island. It is pointed out that although the formation of the island increases the surface energy, but reduces the total energy of the epitaxial layer. The surface energy of slab models is shown in Table 4 and the positive and negative of energy is not considered. It is noted that the surface energy of the slab models is indeed reduced, as in the conclusions of the literature [22].

Table 3. The relationship between two surfaces and interface.

Interface	$\sigma_{Cu}/\text{eV}\cdot\text{\AA}^2$	Relationship	$\sigma_{Ag}/\text{eV}\cdot\text{\AA}^2$
Ag(111)/Cu(111)	1.7461	>	0.9172
Ag(110)/Cu(110)	2.1405	>	1.1357
Ag(100)/Cu(100)	3.0761	>	1.6370

Table 4. The surface properties of slab models.

	Surface	n_{Cu}/n_{Ag}	A (\AA^2)	E_{sur} (eV)
Cu slab	(111)	5/0	5.6585	1.7461
	(110)	10/0	9.2406	2.1405
	(100)	10/0	6.5341	3.0761
Cu/Ag slab	Ag(111)/Cu(111)	5/5	7.7039	0.0006
	Ag(110)/Cu(110)	10/10	9.1618	0.0880
	Ag(100)/Cu(100)	10/10	8.1644	1.5601

3.3. Population Analysis of Interface

Mulliken population refers to the distribution of electrons in each atomic orbit. By analyzing the atomic charge population, the bonding between atoms at the interface and the amount of charge transfer can be known. Table 5 shows the atomic charge population of the interface models. According to the data in the table, the Cu and Ag atoms in each model are positively and negatively charged, and the number of electrons obtained by the Cu atoms is equal to the number of electrons lost by the Ag atoms. It is indicated that Cu atoms transfer electrons to Ag atoms, which form ionic bonds (underlined data). However, the data that is not marked differs greatly, so it can be concluded that there are other bonds or forces in the interface. According to the Mulliken bond population, the values of each group are less than 1, indicating that the Ag-Cu bond contains both covalent bonds and ionic bonds. For the Ag(111)/Cu(111) interface, the Mulliken bond population is close to 0, showing a strong ionic bond property, and it also shows that the interface stability gradually decreases as the crystal face index increases. In other words, with the epitaxial growth of the Ag layer, the stability is gradually reduced, eventually causing the morphology to be unstable, resulting in a rough surface of the material.

Table 5. The atomic charge and Mulliken bond population of Ag(hkl)/Cu(hkl) interfaces.

Species	Ag(111)/Cu(111)		Ag(110)/Cu(110)		Ag(100)/Cu(100)	
	Population	Charge(e)	Population	Charge(e)	Population	Charge(e)
Cu	11.00	0.04/−0.08	11.01	0.03/−0.11	11.01	0.02/−0.09
Ag	10.99	0.04/−0.05	10.99	0.02/−0.03	10.99	0.03/−0.02
Cu-Cu	0.61/−0.64	–	0.54/−0.20	–	0.72	–
Ag-Ag	−0.43	–	0.62/−0.09	–	0.47/−0.19	–
Ag-Cu	0.32	–	0.68	–	0.62	–

3.4. Electronic Structure Analysis of Interface

To investigate the differences in bonding ability, the density of states is calculated where the Fermi level E_F is set at the position of energy $E = 0$ eV, as shown in Figure 3. The E_F of DOS for each model is larger than 0, indicating that both the Ag and Cu slab in the interface system maintain the metallic characteristic. The DOS of the Ag atoms is mainly contributed by the valence electrons of Ag 4d and a small amount of Ag 4p, Ag 5s orbitals, and the DOS of the Cu atoms is mainly contributed by the valence electrons of Cu 3d and a small amount of Cu 3p, Cu 4s orbitals. Except for peak and peak shapes, the density of states of different models is comparable, and the d orbital of the Cu atom overlaps with the d orbital of the Ag atom, resulting in hybridization and a strong interaction. Figure 3d shows the density of states of Cu and Ag atoms in the Ag(100)/Cu(100) model, and the density of states of the Cu and Ag atoms in other interfaces is not given because the stability of Ag(100)/Cu(100) is the highest and the peak is more obvious. It is exhibited that the p orbital of the Cu atom also overlaps with the d orbital of the Ag atom but it is not obvious. Moreover, the charge density distribution and the difference charge density distribution of the interface can show the electron transfer and electron density of interfaces more intuitively. The unit of the values in Figure 4 is all electrons/ \AA^3 . There is a phenomenon of charge accumulation and electron transfer between Cu and Ag, indicating that they are connected by ionic bonds with covalent properties. For the Ag(111)/Cu(111) model, although

Cu and Ag in the vicinity of the interface have common electrons, the density is extremely low, and mainly free electrons are present. Therefore, there is a strong metal bond between Cu and Ag. For the Ag(110)/Cu(110) and Ag(100)/Cu(100) models, the latter exhibits more common electrons and strong covalent bonds. However, the mismatch of the Cu/Ag interface is large (more than 15%), so there are non-bonding forces and strain at the interface, which requires further calculations.

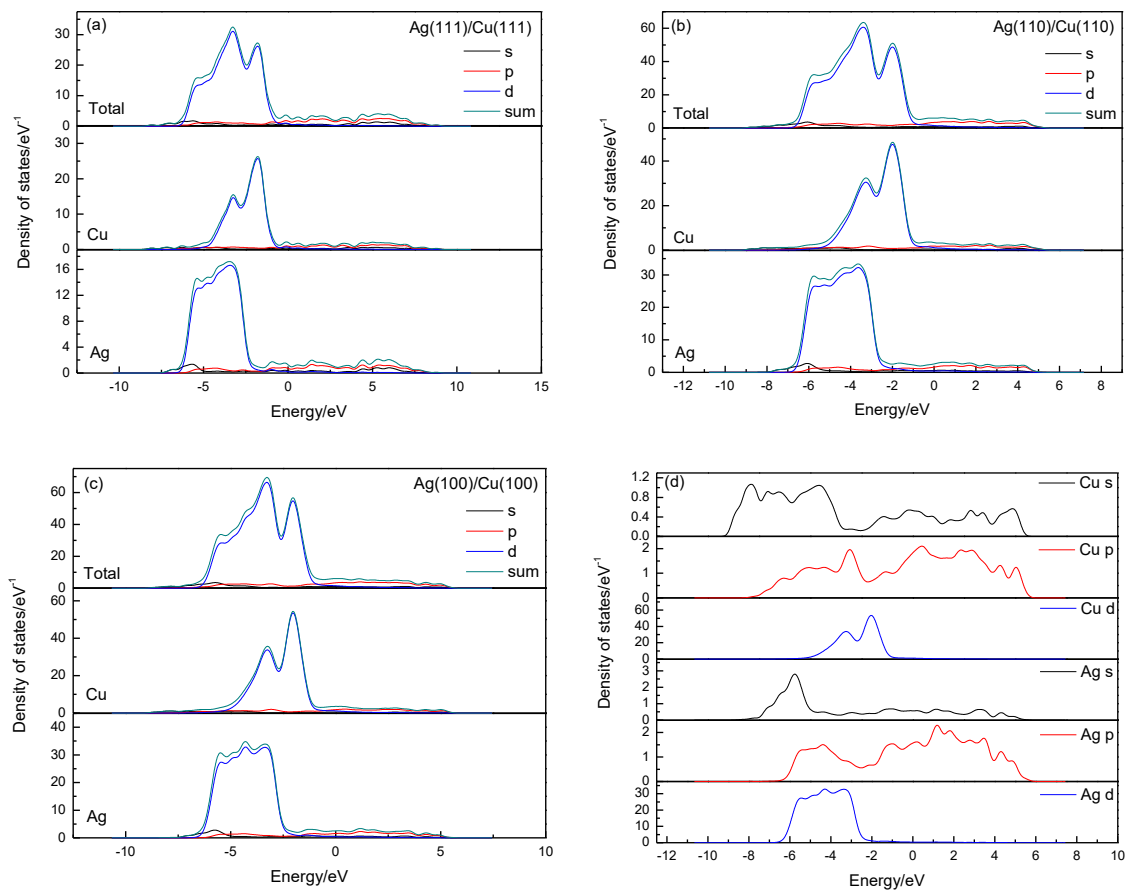


Figure 3. Density of states of the interface of Cu/Ag composite. (a) PDOS of Ag(111)/Cu(111); (b) PDOS of Ag(110)/Cu(110); (c) PDOS of Ag(100)/Cu(100); (d) PDOS of Cu and Ag atoms in Ag(100)/Cu(100).

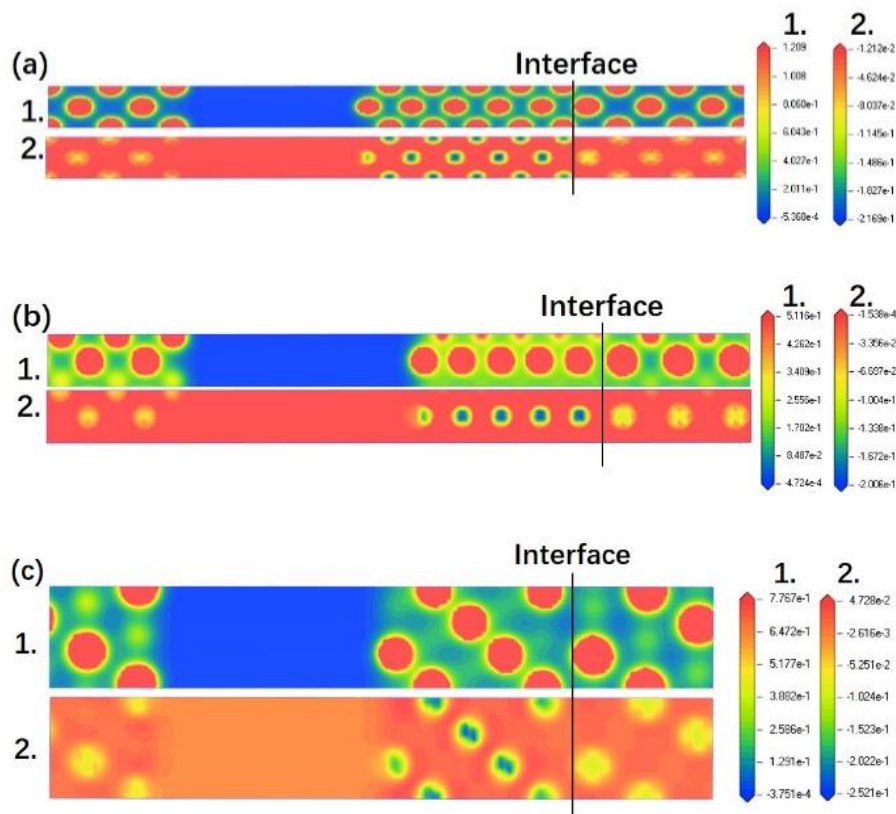


Figure 4. The charge density distribution and the difference charge density distribution of the interface. (a) Ag(100)/Cu(100); (b) Ag(110)/Cu(110); (c) Ag(111)/Cu(111).

3.5. Force Analysis of Interface

To further describe the forces between Cu and Ag, the radial distribution function is calculated, as shown in Figure 5. In all models, there is a maximum in the range of $r < 2.6 \text{ \AA}$, indicating that the bond is the main force that constitutes the interface. However, for the Ag(100)/Cu(100), there also peaks with high peaks in the range of $2.6\text{--}3.1 \text{ \AA}$, indicating that there are strong hydrogen bonds in the interface. Besides, there are also peaks in the range of $r > 3.1 \text{ \AA}$, exhibiting Van der Waals force [23].

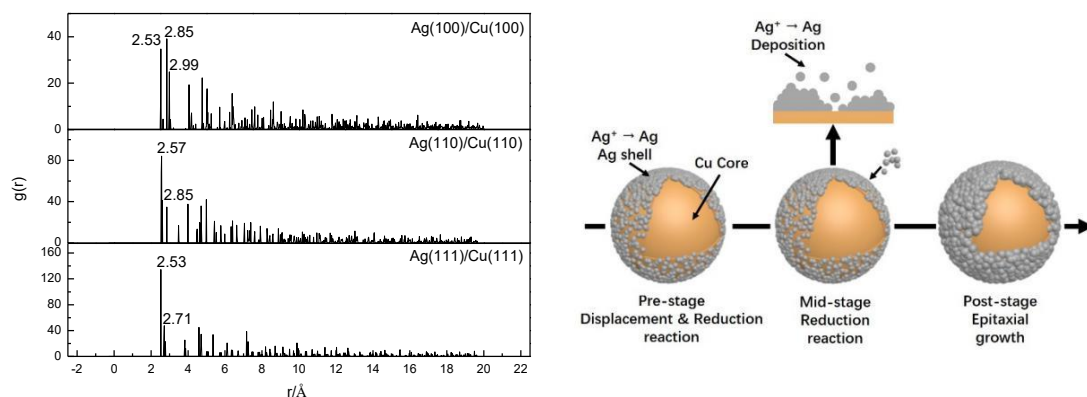


Figure 5. The radial distribution function of interface and the three-dimensional schematic diagram.

According to the above conclusion, the growth mode of the Ag coating can be inferred, and the three-dimensional schematic diagram is also as shown in Figure 5. The growth of the Ag coating is mainly composed of three stages.

Pre-stage: The displacement reaction and the direct reduction reaction occur simultaneously in the solution, but since the surface energy of each surface of Cu differs, the reactivity of each surface also differs, resulting in the formation of vacancies and a thin layer of Ag on the Cu surface.

Min-stage: As the direct reaction of Ag continues, the Cu surface is covered by Ag and the vacancies disappear. When the coating reaches a certain thickness, the strain energy of each surface is released outward, resulting in irregular protrusions on the surface of the composite.

Post-stage: As the reaction progresses, the Ag^+ ion concentration in the solution gradually decreases, the reaction reaches equilibrium, and the growth of the Ag coating stops.

Regarding the core of a regular geometry, especially two elements (such as Pb and Pt) that differ by one period from the periodic table, the conclusions reached are similar. The growth of the shell is divided into two stages, that is, the shell grows epitaxially, and then the island grows. The difference is that the simulation calculation and characterization of core-shell particles with a spherical structure are more complex, and are easily affected by external factors during the synthesis [24]. In this paper, calculations and characterizations confirm each other, indicating that the method is credible.

4. Conclusions

Cu/Ag core-shell composite can be synthesized by the replacement-reduction method. According to the characterization results, the depositing of the Ag coating increases the particle size, and there are irregular protrusions on the surface of the particles. To investigate the growth mode of the Ag coating, the first-principles calculation is used to analyze the Ag/Cu interface structure to infer the growth mode of the Ag coating. It is found that the growth mechanism of the Ag coating belongs to the Stranski–Krastranow (SK) mode and is divided into three steps. Since the Ag/Cu interface contains bonds, hydrogen bonds, and van der Waals forces, the bond strength between the coating and the substrate is weak, but this result is not obvious in the early growth stage. As the thickness of the coating increases, the particle must reduce the surface energy to reach equilibrium. Therefore, the strain energy generated by the lattice mismatch at the interface must be released, eventually leading to irregular protrusions on the surface of the particle. The core-shell composite synthesized according to the SK mode can greatly reduce defects due to lattice mismatch. At the same time, this research method is also applicable to more complex core-shell composites, and also provides theoretical support for the preparation and modification of core-shell composites.

Author Contributions: Conceptualization, X.W. and Y.W.; methodology, J.L. (Jinlin Lu); software, X.W.; validation, X.W., Z.N. and J.L. (Jidong Li); formal analysis, X.W. and Y.W.; funding acquisition, Y.W. All authors have read and agreed to the published version of the manuscript.

Funding: This research was funded by National Natural Science Foundation of China (51674141), University of Science and Technology Liaoning Graduate Education Reform and Technology Innovation and Entrepreneurship Project (LKDYC201901), University of Science And Technology Liaoning Talent Project Grants (601011507-14).

Conflicts of Interest: There are no conflicts of interest to declare.

References

1. Nagahama, C.; Zinchenko, A. Small DNA additives to polyelectrolyte multilayers promote formation of ultrafine gold nanoparticles with enhanced catalytic activity. *Colloid Polym. Sci.* **2019**, *297*, 363–369. [[CrossRef](#)]
2. Zhu, B.; Li, K.; Feng, Y.; Zhang, S.; Wu, S.; Huang, W. Synthesis and catalytic performance of gold-loaded TiO_2 nanofibers. *Catal. Lett.* **2007**, *118*, 55–58. [[CrossRef](#)]
3. Mei, Y.; Sharma, G.; Lu, Y.; Ballauff, M.; Drechsler, M.; Irrgang, T.; Kempe, R. High catalytic activity of platinum nanoparticles immobilized on spherical polyelectrolyte brushes. *Langmuir* **2005**, *21*, 12229–12234. [[CrossRef](#)] [[PubMed](#)]
4. Hillier, A.C.; Grasa, G.A.; Viciu, M.S.; Lee, H.M.; Yang, C.I.; Nolan, S.P. Catalytic cross-coupling reactions mediated by palladium/nucleophilic carbene systems. *J. Organomet. Chem.* **2002**, *653*, 69–82. [[CrossRef](#)]
5. Xie, W.; West, D.J.; Sun, Y.; Zhang, S. Role of nano in catalysis: Palladium catalyzed hydrogen desorption from nanosized magnesium hydride. *Nano Energy* **2013**, *2*, 742–748. [[CrossRef](#)]

6. Choudary, B.M.; Madhi, S.; Chowdari, N.S.; Kantam, M.L.; Sreedhar, B. Layered double hydroxide supported nanopalladium catalyst for Heck-, Suzuki-, Sonogashira-, and Stille-type coupling reactions of chloroarenes. *J. Am. Chem. Soc.* **2002**, *124*, 14127–14136. [[CrossRef](#)]
7. Hickman, A.J.; Sanford, M.S. High-valent organometallic copper and palladium in catalysis. *Nature* **2012**, *484*, 177–185. [[CrossRef](#)]
8. Tegoua, A.; Papadimitriou, S.; Pavlidou, E.; Kokkinidisa, G.; Sotiropoulos, S. Oxygen reduction at platinum- and gold-coated copper deposits on glassy carbon substrates. *J. Electroanal. Chem.* **2007**, *608*, 66–77. [[CrossRef](#)]
9. Peng, Y.; Yang, C.; Chen, K.; Popuri, S.R.; Lee, C. Study on synthesis of ultrafine Cu–Ag core–shell powders with high electrical conductivity. *Appl. Surf. Sci.* **2012**, *263*, 38–44. [[CrossRef](#)]
10. Meng, Z.H.; Xie, K.N.; Liao, L.; Li, Y.J. Preparation and characterization of Ag-Cu coated powder. *J. Funct. Materials* **2013**, *11*, 1656–1662.
11. Nian, P.; Li, Y.; Zhang, X.; Cao, Y.; Liu, H.; Zhang, X. ZnO Nanorod-induced heteroepitaxial growth of SOD type Co-based zeolitic imidazolate framework membranes for H₂ separation. *ACS Appl. Mater. Inter.* **2018**, *10*, 4151–4160. [[CrossRef](#)]
12. Shi, Z.; Li, H.; Yuan, Q. Van der waals heteroepitaxial growth of monolayer Sb in a puckered honeycomb structure. *Adv. Mater.* **2018**, *31*, 1806130. [[CrossRef](#)] [[PubMed](#)]
13. Weng, W.; Hsu, C.; Lee, J.; Fan, H.; Liao, C. Twin-mediated epitaxial growth of highly lattice-mismatched Cu/Ag core–shell nanowires. *Nanoscale* **2018**, *10*, 9862–9866. [[CrossRef](#)] [[PubMed](#)]
14. Khoo, K.H.; Arantes, J.T.; Chelikowsky, J.R.; Dalpian, G.M. First-principles calculations of lattice-strained core-shell nanocrystals. *Phys. Rev. B* **2011**, *84*, 075311. [[CrossRef](#)]
15. Kong, X.; Wang, J. Copper(II) adsorption on the kaolinite(001) surface: Insights from first-principles calculations and molecular dynamics simulations. *Appl. Surf. Sci.* **2016**, *389*, 316–323. [[CrossRef](#)]
16. Lee, T.K.; Chiang, C.S.; Lee, W.H. A study on Cu particles coated with nano-silver by a replacement reaction between silver nitrate and copper particles. *J. Nanosci. Nanotechnol.* **2017**, *17*, 4157–4161. [[CrossRef](#)]
17. Kim, J.J.; Lee, H.W.; Dabhade, V.V.; Kim, S.R.; Kwon, W.T.; Choi, D.J.; Kim, H.; Kim, Y. Electro magnetic interference shielding characteristic of silver coated copper powder. *Met. Mater. Int.* **2010**, *16*, 469–475. [[CrossRef](#)]
18. Ledentsov, N.N.; Shchukin, V.A.; Grundmann, M.; Kirstaedter, N.; Böhrer, J.; Schmidt, O.; Bimberg, D.; Ustinov, V.M.; Egorov, A.Y.; Zhukov, A.E.; et al. Direct formation of vertically coupled quantum dots in Stranski-Krastanov growth. *Phys. Rev. B* **1996**, *54*, 8743. [[CrossRef](#)]
19. Zhao, X.; Zhuo, Y.; Liu, S.; Zhou, Y.; Zhao, C.; Wang, C.; Yang, Q. Investigation on WC/TiC interface relationship in wear-resistant coating by first-principles. *Surf. Coat. Technol.* **2016**, *305*, 200–207. [[CrossRef](#)]
20. Yang, D.; Liu, H.; Liu, L.; Sarina, S.; Zheng, Z.; Zhu, H. Silver oxide nanocrystals anchored on titanate nanotubes and nanofibers: Promising candidates for entrapment of radioactive iodine anions. *Nanoscale* **2013**, *5*, 11011–11018. [[CrossRef](#)]
21. Antanobich, A.; Achtstein, A.; Matsukovich, A.; Prudnikau, A.; Bhaskar, P.; Gurin, V.; Molinari, M.; Artemyev, M. Strain-induced exciton transition energy shift in CdSe nanoplatelets: The impact of the organic ligand shell. *Nanoscale* **2017**, *9*, 18042–18053. [[CrossRef](#)] [[PubMed](#)]
22. Attard, G.A. A phenomenological theory of electrosorption. *Electroanal. Chem.* **2018**, *819*, 481–494. [[CrossRef](#)]
23. Kellerman, D.; Medvedeva, N.; Mukhina, N.; Semenova, A.; Baklanova, I.; Perelyaeva, L.; Gorshkov, V. Vanadium doping of LiMnPO₄: Vibrational spectroscopy and first-principle studies. *Chem. Phys. Lett.* **2014**, *591*, 21–24. [[CrossRef](#)]
24. Xiong, Y.; Ma, Y.; Li, J.; Huang, J.; Yan, Y.; Zhang, H.; Wu, J.; Yang, D. Strain-induced Stranski-Krastanov growth of Pd@Pt core-shell hexapods and octapods as electrocatalysts for methanol oxidation. *Nanoscale* **2017**, *9*, 11077–11084. [[CrossRef](#)]

